Cobalt-Iron Decorated Tellurium Nanotubes for High Energy Density Supercapacitor

Prangya Bhol,[a] Swarnalata Swain,[a] Ali Altaee,[b] Manav Saxena,[a]

Akshaya K. Samal[a]

[a]Centre for Nano and Material Sciences, Jain University, Jain Global Campus,

Ramanagara, Bangalore 562112, India

[b]Centre for Green Technology, School of Civil and Environmental Engineering,

University of Technology Sydney, 15 Broadway, NSW 2007, Australia

*Email: s.akshaya@jainuniversity.ac.in

ABSTRACT

We report the synthesis of cobalt-iron (Co-Fe) decorated tellurium nanotubes (Te NTs) using semiconductive Te NTs as a sacrificial template using the wet chemical method. The Co and Fe precursor concentration incorporated into Te NT plays a significant role in obtaining various bimetallic telluride structures. The one-dimensional (1-D) structure of Co-Fe decorated Te NTs with Te NTs in the backbone provides superior conductivity and exhibits high electrochemical performance with battery type electrode behaviour. The Co-Fe decorated Te NTs electrode is combined with the electric double-layer capacitors (EDLC) type electrode activated carbon (AC) to tune the energy density performance. The asymmetric assembly shows an excellent specific capacitance of 179.2 F g^{-1} (48.7 mAh g^{-1}) at a current density of 0.9 A g^{-1} in 4 M KOH electrolyte. More importantly, it exhibits a maximum energy density of 62.1 Wh Kg^{-1} at a power density of 1138.2 W Kg^{-1} under a potential window of 1.58 V. This potential finding shows the significant applicability of Te NTs as a template for the synthesis of bimetallic tellurides with unique

morphologies. The synergistic effect from multimetals and anisotropic morphology is beneficial for energy storage applications.

1. INTRODUCTION

1-D nanomaterials have congregated worldwide attention in the development of nanomaterial-based various applications. Anisotropic nanostructures such as nanorods, nanowires, and nanotubes have displayed novel or improved properties, and these properties can be tuned based on specific characteristics such as length, distribution, and diameter [1,2]. Engineering of monodispersed shape, size, and morphology-controlled nanostructures still is a great challenge, and diverse routes have been followed to achieve anisotropic nanostructures [3,4]. In recent years, significant efforts have been made to design 1-D nanomaterials that unlock a plethora of promising applications such as electronics and optoelectronics and open up a new platform of fundamental understanding of the structure-property correlation [5,6].

The supercapacitor has recently received prime recognition as an energy storage device owing to its high specific capacitance, excellent cyclic stability, and short charging time [7,8]. The supercapacitor's working mechanism is classified into EDLC and battery type pseudocapacitors [9]. When a hybrid supercapacitor (HSC) is created by combining the EDLC and battery type electrode behavior, it demonstrates captivating characteristics with phenomenal energy storage capacity [10,11]. Broadening the potential window, huge power density, and energy density are some of the perceptible advantages HSCs have received because of the coupling of the dissimilar

positive and negative electrodes [12]. Transition metal oxides/hydroxides/chalcogenides are suitable options for electrode materials due to high specific capacitance and energy density based on the surface Faradaic redox mechanism [13]. To surmount the conductivity issue in the transition metal oxide electrodes, these are substituted with transition metal chalcogenides (TMCs) such as metal sulfides, selenides, and tellurides, which offers enhanced electrical conductivity with excellent electrochemical properties. TMCs could function as mixed conductors and could be moulded into any desired anisotropic nanostructure, because of which it drew a lot of attention [14]. Considering the advantages, it could be easily fabricated into any pre-required architecture with high surface area and porosity that could provide excellent properties beneficial for energy storage mechanism [15,16].

In addition to these advantages, the core electronic structure of metal chalcogenides can be manipulated by the appropriate addition of multiple metals strengthening the electrical conductivity and enabling better charge storage performance [17]. Individual layers comprising metals covalently bonded to chalcogenide atoms grow along one direction by weak van der Waals force of interaction sandwiched one upon another to build a multilayered morphology [18]. Metal sulfides and selenides-based nanomaterials such as CuS, CoS, $ZnCoS$, $MnCoS$, $NiCoSe_2$, $NiCoS$, and others have been extensively researched in the energy storage field to date [19-24]. When a monometal sulfide/selenide-based electrode is extended to a mixed metal sulfide/selenide-based electrode, it potentially increases its efficacy in the energy storage application due to increased electrical conductivity and active participation of multi-metals in the redox reaction.

Te is one of group sixteen periodic table elements in the transition from metal to nonmetal with similar properties like sulfur and selenium. It possesses a high conductivity of 10×10^3 S m^{-1} and

a p-type fine band gap of 0.35 eV, which is expected to deliver better electrochemical performance [25,26]. Te holds an exceptional helical chain-like configuration in its crystal lattice with anisotropic growth tendency along (001) plane crystallographic direction [27]. Despite metal tellurides possessing noteworthy advantages compared to metal sulfide/selenide, these are not explored much in the range of energy storage. Newly Te-based electrodes are being studied for supercapacitor application; for example, a binder-free approach was used to prepare NiTe, which showed a specific capacitance of 804 F g^{-1} at 1 A g^{-1} current density [28]. The authors assembled NiTe as a cathode in an asymmetric setup. The anode was AC, which worked in the potential range of 1.6 V, delivering an energy density of 34 Wh Kg^{-1} at a power density of 807 W Kg^{-1}. In another study, CoTe//AC asymmetric supercapacitor assembled via hydrothermal technique, providing a capacitance value of 622.8 F g^{-1} at 1 A g^{-1} [29]. $MoTe_2$ was successfully synthesized by Liu and his group using the colloidal chemistry approach. The electrode was successfully achieved elevated specific capacitance of 1393 F g^{-1} at 1 A g^{-1} [18]. Iron telluride based supercapacitor was successfully synthesized, FeTe: Fe_2TeO_5 thin films by following a successive ionic layer adsorption reaction process [30]. The material showed a specific capacitance of 591 F g^{-1} at 3 mV s^{-1}. Yu et al. fabricated WTe_2 nanosheet as electrode material which showed capacitance of 221 F g^{-1} at 1 A g^{-1} [31]. However, most of these studies involved monometallic telluride nanostructures whose working efficiency can be triggered by coupling them with bimetals, offering amazing redox reactions and storing profuse charges.

Bimetallic/ multi-metallic tellurides have been recently reported to show enhanced properties and benefits compared to monometallic tellurides such as NiCoTe [32], NiFeTe [33] and shown better performance. Hence, there is room for new materials with unique morphology by selecting the correct pair of bimetals that could show enhanced electrochemical characteristics. Fe-based

materials have potentially been used to fabricate electrode materials based on the benefits of rich redox activity, low cost, environmentally friendly, and high abundance in the Earth's crust [34-35]. The only disadvantage of Fe that prevents it from being fully utilized in energy storage applications is its low conductivity [36]. To overcome the conductivity issue, it could be hybridized with conducting materials like Co, Te or both, which are expected to show high conductivity and enhance the performance in supercapacitor.
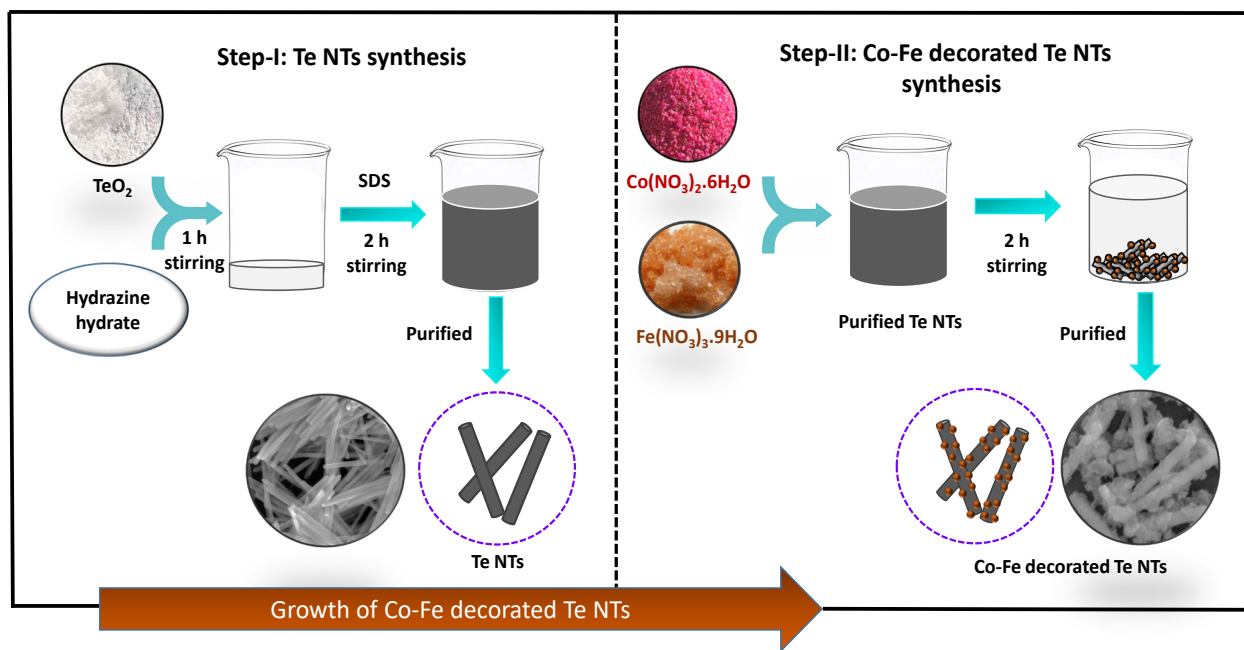

Fig. 1. Illustration of methodology for the preparation of Co-Fe decorated Te NTs.

Based on the previous studies, it is necessary to synthesize mixed metal tellurides for supercapacitor application. We synthesized Co-Fe decorated Te NTs using Te NTs as the template. Fig. 1 illustrates the overall work scheme for synthesizing Co-Fe decorated Te NT electrode on Ni foam. First, Te NTs were synthesized and employed as a sacrificial template in the synthesis. Afterwards, Co/Fe was decorated on the sacrificial template. The growth of Co/Fe nanoparticles (NPs) on Te NTs was optimized using different metal ratios. Rich electroactivity from Co-Fe

bimetallic, the conductivity of Te, and tubular morphology with rougher bulges on the surface all together contribute to show excellent electrochemical performance. The specific capacitance of 1119.2 F g^{-1} (88.3 mAh g^{-1}) at a current density of 6 A g^{-1} was obtained from Co-Fe decorated Te NTs. The Co-Fe decorated Te NTs electrode was assembled in an asymmetric setup with AC for real-time application. The CoFeTe-2//AC persuaded a high energy density of 62.1 Wh Kg^{-1} at a power density of 1138.2 W Kg^{-1}.

2. MATERIALS AND METHODS

Sodium dodecyl sulfate (SDS), $C_{12}H_{25}NaSO_4$, was purchased from MERCK, India. Tellurium dioxide (TeO_2) powder, Cobalt (II) nitrate hexahydrate ($Co(NO_3)_2.6H_2O$) and Iron (III) nitrate nonahydrate ($Fe(NO_3)_3.9H_2O$) were purchased from SRL, India. Hydrazine hydrate ($N_2H_4 \cdot H_2O$) was from Qualigens, India. Potassium hydroxide (KOH) was from SD FINE chemicals, India. Instrument details with respect to the analysis used for material characterization have been summarized in the supporting information (SI).

3. EXPERIMENTAL SECTION

3.1. Synthesis of Te NTs

TeO_2 (64 mg) mixture in 20 ml hydrazine hydrate was first magnetically stirred for 1 h at room temperature. The reaction color changes to blackish-blue within 1 h, indicating the formation of Te NTs. Afterwards, the reaction was diluted 10 times with 10 mM SDS solution and continued for stirring for another 2 h. Throughout the reaction, the stirring rate was maintained at ~400 rpm. Then, the synthesized Te NTs were cleaned twice by centrifuging at 6000 rpm for 10 min. After cleaning, the total volume was adjusted to 200 mL with DI water.

3.2. Synthesis of Cobalt-Iron decorated Te NTs

The Co-Fe decorated Te NTs were synthesized using a wet chemical approach. At first, the prepared Te NTs solution served as the sacrificial template, and the precursors of Co and Fe were mixed with the synthesized Te NTs solution. Table 1 represents the Co/Fe precursor concentrations used for synthesizing three different samples with variable (metal (Co+Fe): Te precursor) ratios, i.e., 1:12, 1:6, 1:3. The mixture was magnetically stirred for a continuous 2 h with a stirring speed of 450 rpm. Later, it was allowed to precipitate overnight. The precipitate was collected and redispersed with water and centrifuged twice at 3000 rpm to remove unnecessary ions. Ultimately, Co-Fe decorated Te NTs were obtained by drying in an oven at 65 °C for overnight.

Table 1

Precursors, $Co(NO_3)_2.6H_2O$ and $Fe(NO_3)_3.9H_2O$ quantity added to the synthesized Te NTs

Co-Fe decorated Te NTs (M:Te)	Te NTs (mL) solution (2 mM)	$Co(NO_3)_2.6H_2O$ (mM)	$Fe(NO_3)_3.9H_2O$ (mM)
CoFeTe-1 (1:12)	200	0.13	0.03
CoFeTe-2 (1:6)	200	0.27	0.06
CoFeTe-3 (1:3)	200	0.54	0.12

3.3. Electrochemical testing and fabrication of electrode

Three-electrode system: The electrodes were framed by the slurry deposition method. 1 mg of active material, 95 µL ethanol and 5 µL Nafion were mixed with ultrasonication for 10 min and poured dropwise on top of cleaned Ni Foam (~0.5 cm^2). Afterwards, the electrodes were kept in

an oven at 65 °C for 6 h. The dried electrode was pressed with 5 tons of pressure and carried out for further electrochemical investigation. The experiments were carried out in 4 M KOH using Pt wire as an auxiliary electrode, Ag/AgCl as a reference electrode, and Co-Fe decorated Te NTs as a working electrode. The specific capacitance of the framed electrode on Ni foam was measured from CV and GCD curves following the equation 1-2 [37].

Two-electrode system: The asymmetric setup of CoFeTe-2 with AC was assembled as positive and negative electrodes, respectively CoFeTe-2//AC. CoFeTe-2 and AC slurry were framed on two rounds of Ni foam with the prementioned method in the 3-electrode system section. The deposited foam samples were dried for 6 h at 65 ⁰C. For device fabrication, a Swagelok cell was used in which Whatman filter paper served as a separator sandwiched between the two electrodes. Specific capacitance for CoFeTe-2 was measured using CV curves and GCD cycles using equations (1) and (2), and specific capacity for CoFeTe-2 was calculated using GCD curves using equation (3) [37].

$$C_{sp} = [2 \times m \times s \times \Delta V]^{-1} \int i(V)dV \qquad (1)$$

$$C_{sp} = \frac{i \times \Delta t}{m \times \Delta V} \qquad (2)$$

$$Q = \frac{i \times \Delta t}{m} \qquad (3)$$

In which, specific capacitance is represented as C_{sp} (F g⁻¹), curve area is the integrated portion of equation 1, Q (mAh g⁻¹) signifies specific capacity, "s" (mV s⁻¹) for scan rate, "m" (g) for the added mass of electrode material, "i" (A) for current, "ΔV" (V) represents operating potential window and "Δt" (s) corresponds to discharge time. The energy density and power density values

were measured from equations (4) and (5). "E" (Wh Kg^{-1}) represents energy density, and "P" (W Kg^{-1}) represents the power density in the following equations.

$$E = \frac{1}{2} \times C_{sp} \times \Delta V^2 \qquad (4)$$

$$P = \frac{E}{\Delta t} \qquad (5)$$

4. RESULTS AND DISCUSSION

A two-step synthesis method is followed to prepare Co-Fe decorated Te NTs. A self-sacrificial Te NT template is initially prepared following a wet chemical approach at room temperature. Hydrazine hydrate was added in the first step of the reaction to reduce the Te precursor as well as provide an alkaline medium in the solution. SDS caps and stabilizes the Te NTs and helps to grow in one direction. In the reaction, the h-Te nanocrystalline seed grows into Te NTs by following a solid-solution-solid (SSS) transformation mechanism [38,39]. In the second step, Te NTs functions as a self-sacrificing template. The surface of the sacrificial template Te NTs was decorated with Co/Fe NPs by treating with different concentrations of Co and Fe precursors, resulting in three distinct morphologies. The reaction was stirred magnetically for 2 h, and Co-Fe decorated Te NTs were formed. The obtained materials were further characterized with various techniques to determine their structural and electrochemical properties.

4.1. Characterization

UV, FESEM and TEM analysis characterized the sacrificial Te NTs template. Two distinct Te peaks were observed in the UV-Vis analysis (Fig. 2A) for Te NTs, in which the absorption at 287 nm (peak I) corresponds to the transition from the p-bonding valence band (VB2) to the p-

antibonding conduction band (CB1) and the absorption at 705 nm (peak II) is because of transition from the p-lone pair valence band (VB3) to the p-antibonding conduction band (CB1) [38-40]. The morphological study of Te NTs was carried out using FESEM and TEM analysis. FESEM image (Fig. 2B) with low magnification confirms the even growth of Te NTs. The NTs were highly monodispersed with tubular morphology. From Fig. 2C, the length of different Te NTs was measured, confirming the NT could grow up to an edge length of ~420 $\pm$ 50 nm with a diameter of ~30 $\pm$ 5 nm. To determine the spacing between the fringes of CoFeTe-2, high-resolution transmission electron microscopy (HRTEM) and selected area electron diffraction (SAED) patterns were followed. Fig. 2D shows the HRTEM image of single Te NT. Fig. 2E is the enlarged area selected from Fig. 2D. The interplanar spacing is ~0.59 nm measured from lattice fringes of the selected square, which matches with the crystal plane (001), depicting the growth of Te is along <0001> direction [41-44]. The SAED pattern was surveyed to determine the crystallinity of Te NTs. Inset in Fig. 2E reveals that the Te NTs synthesized by the wet chemical method are purely single crystals with even morphology. Interplanar spacing measured from the SAED pattern matches with the planes of (100), (102) and (110) of Te (ICDD reference no. 01-079-0736). Fig. 2F shows the EDX pattern obtained from prepared Te NTs, corresponding peaks obtained which matches with Te confirming the existence of Te.

The sacrificial template role of synthesized Te NT was well understood when treated with different bimetallic concentrations of Co^{2+} and Fe^{3+} with a reaction time of 2 h resulting in Co-Fe decorated Te NTs. The synthesized materials were further characterized by FESEM, TEM, XRD, XPS and BET analysis. FESEM analysis clearly shows the growth of Co/Fe NPs on Te NTs. The bare Te NTs possessed a clean surface, as shown in Fig. 3A. However, treating it with Co^{2+} and Fe^{3+} altered the surface morphology into a rougher bulge because of the growth of Co/Fe NPs on Te NTs. The

concentration of Fe was kept less as compared to Co in the reaction because Co-based materials are more electrochemically active and are easy to design into desired shapes. In contrast, Fe-based materials possess a major drawback like low conductivity, which could hamper the electrochemical performance [42,36].
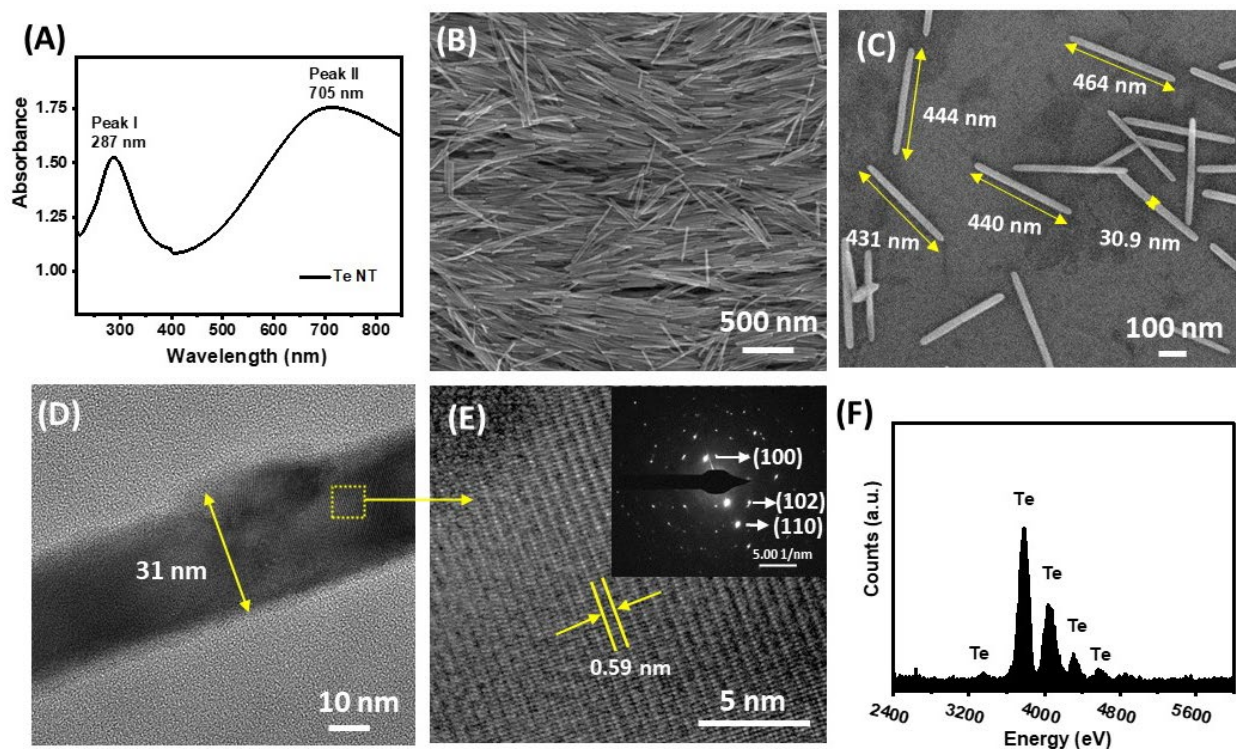

Fig. 2. (A) UV-Vis. spectrum displaying two characteristics peak of Te in Te NTs, (B-C) FESEM image of Te NTs, (D) magnified TEM image showing diameter of Te NT, (E) lattice resolved HRTEM of the selected square from (D), inset shows SAED pattern of Te NT, and (F) EDX pattern of prepared Te NTs.

The slow rise in the Co/Fe concentration added to Te NTs, causes a greater number of NPs to grow on the top of Te NT. Fig. 3B-D shows the morphological change observed from the sample of Te NT to CoFeTe-3 when the concentration of Co/Fe treatment with Te NTs is increased. The tubular structure of Te does not alter during the development of the Co/Fe NPs; in alternation, there is a

rise in the exposed surface area resulting in a greater number of electroactive spots, which could be beneficial for electrochemical performances.
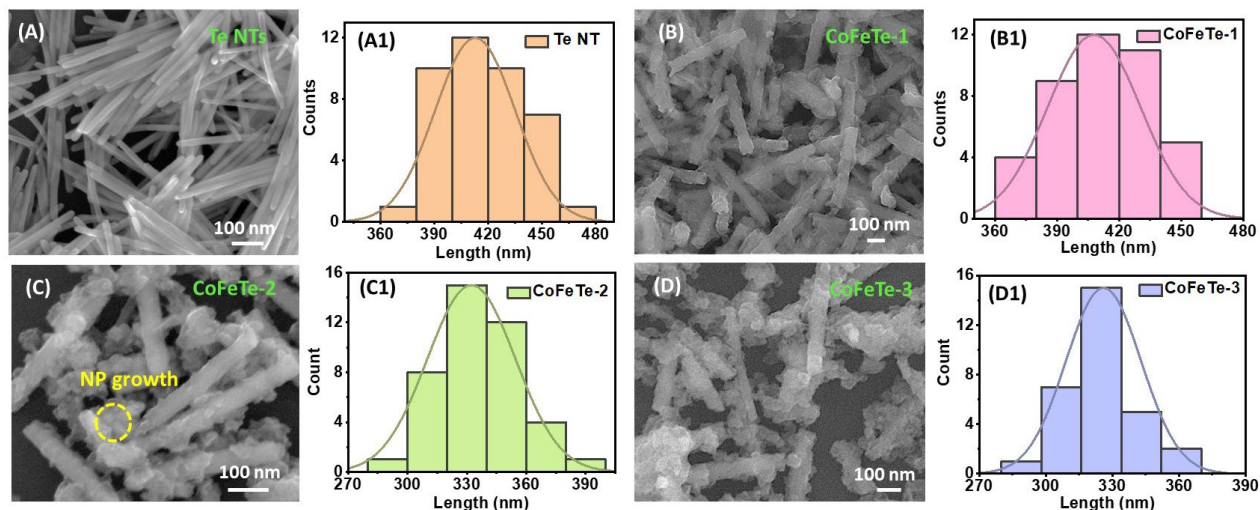

Fig. 3. FESEM images of (A) bare Te NTs, (B-D) CoFeTe-1, CoFeTe-2, and CoFeTe-3 show a steady growth of Co/Fe NPs over Te NT template, and their corresponding histograms are shown from A1 to D1.

The gradual conversion and morphological arrangement of Te NTs to CoFeTe-1, CoFeTe-2 and CoFeTe-3 were well examined using respective FESEM images. The length of synthesized samples revealed by the corresponding histogram plots (Fig. 3B1-D1) was calculated from the FESEM images. Histogram plot obtained (Fig. 3A1) from FESEM image of Te NTs (Fig. 3A) shows the parent Te NTs template grew into an edge length of ~420 ± 50 nm with a diameter of ~30 ± 5 nm. CoFeTe-1 shows a length of ~420 ± 50 nm, which was similar to the length of template Te NT; however, the surface of CoFeTe-1 becomes rougher compared to its starting Te NTs. When the Co^{2+} and Fe^{3+} concentration was further increased, we observed a decrease in the edge length of CoFeTe-2, i.e., ~340 ± 50 nm and a greater number of NPs growth over the surface. Finally, at a high concentration of Co^{2+} and Fe^{3+} (CoFeTe-3), the edge length becomes ~320 ± 50

nm with a width of 70$\pm$ 5 nm. The variation of morphology originates because of the rapid reaction of Co^{2+} and Fe^{3+} on top of the surface of template Te NTs.

The detailed morphological analysis of CoFeTe-2 was done using FESEM and TEM analyses. Fig. 4A confirms each of the CoFeTe-2 grew uniformly with tubular shape. Moreover, the tubular morphology of CoFeTe-2 was clearly evidenced from high-resolution TEM (HRTEM) image of CoFeTe-2 given in the Fig. S1 of SI. Fig. 4B reveals the clear growth of Co/Fe NPs on Te NTs surface. HRTEM image of CoFeTe-2 obtained from the selected area of Fig. 4B shows the fringe spacing (Fig. 4C). The interplanar spacing measured from various spots matches with the (001) plane of Te (ICDD reference no. 01-079-0736), (100) plane of Co (ICDD reference no. 00-001-1278), (002) plane of Fe (ICDD reference no. 00-034-0529). The SAED pattern (Fig. 4D) was followed to envisage the crystallinity of CoFeTe-2, and it revealed that the synthesized CoFeTe-2 is purely crystalline with even morphology. The interplanar spacing (d) was calculated from the SAED pattern spots that match with the (001) and (111) planes of Te nanocrystal matched with (ICDD reference no. 01-079-0736).

EDX spectrum shown in Fig. 4E confirms the existence of Co, Fe, and Te. In addition to that, Cu and C peaks were obtained since sample preparation was on a carbon-coated copper grid for TEM analysis. The additional peak of S obtained due to surfactant SDS capping to the Te NTs, and the peak of O may be due to the surface oxidation of Te NTs during sample preparation. Fig. 4F shows a high angle annular dark-field (HAADF) image of CoFeTe-2, revealing Te NT to be present in the pristine backbone with the formation of Co/Fe NPs on Te NT surface. Elemental mapping was carried out to determine the distribution of Co, Fe and Te in the synthesized CoFeTe-2. The mapping clearly shows the Te NT was intact with tubular morphology providing a backbone to

grow Co/Fe NPs as shown in Fig. 4G. As evident from Fig. H-I. Co was homogenously distributed inside the Te NT, forming an alloy with Te and getting decorated on the surface of Te NT, while in the case of Fe, it majorly resided at the surface of Te NT.
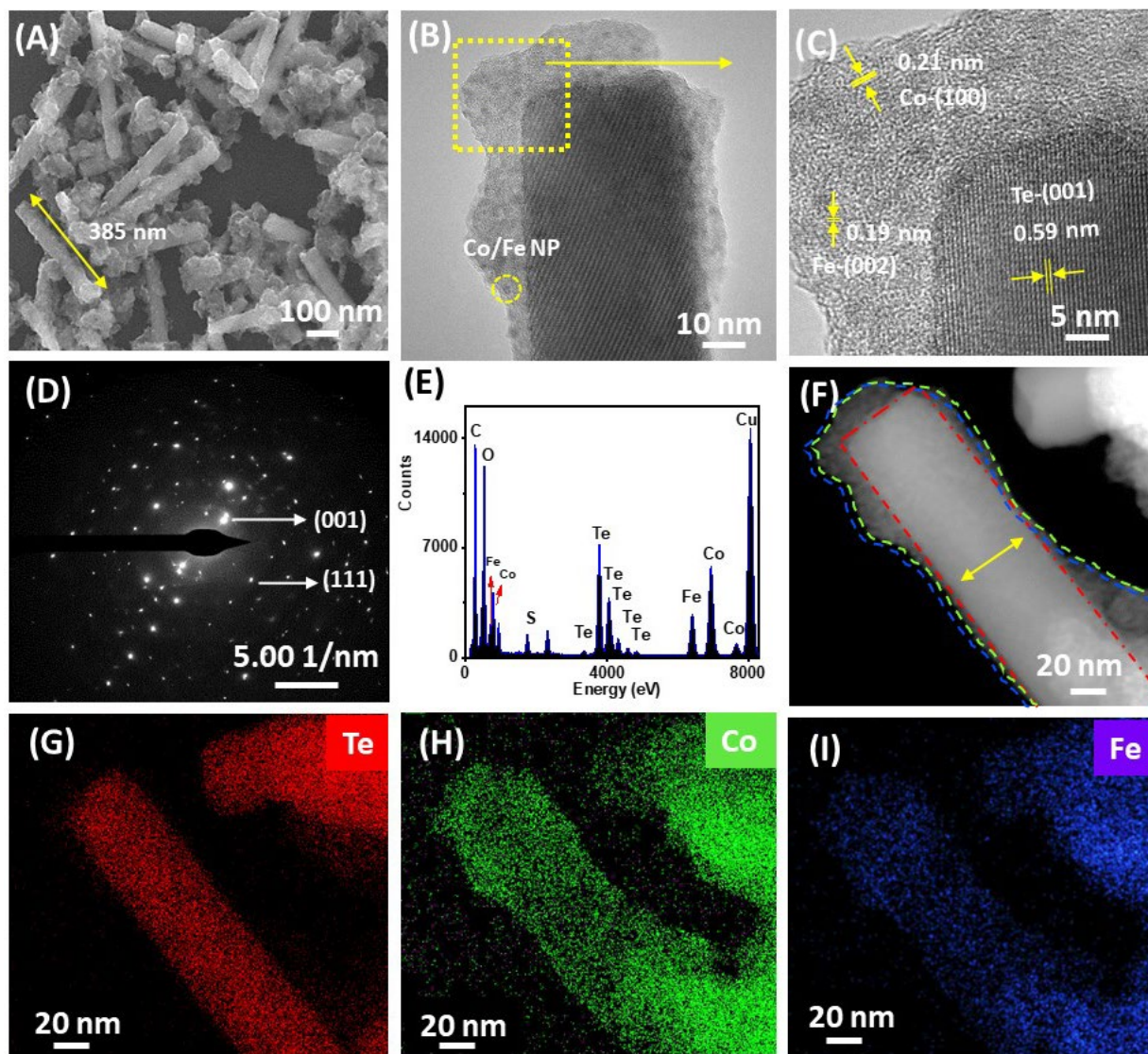

Fig. 4. (A) FESEM images of CoFeTe-2 NTs, (B) TEM image of CoFeTe-2 NT shows the growth of Co/Fe NPs, (C) HRTEM image of CoFeTe-2 NT, (D) SAED pattern of CoFeTe-2 NTs, (E) EDX of CoFeTe-2 NTs, (F) HAADF image of CoFeTe-2 and (G-I) EDS element mappings of Te, Co and Fe, respectively present in CoFeTe-2 NTs.

To determine the crystallography of the obtained products, PXRD was carried out. Fig. 5A shows XRD patterns for Te NT and CoFeTe-2. In the XRD pattern the peaks at 2θ, the values obtained are 22.9, 27.4, 38.1, 40.4, 43.4, 45.9, 49.5, 51.3, 52.0, 56.9, 62.8, 65.9, 67.7, and 72.0 matches with the plane (100), (011), (102), (110), (111), (003), (201), (112), (103), (022), (113), (121) (014), and (212), respectively of hexagonal crystal arrangement of Te with unit cell constants of a = 0.44 nm and c = 0.59 nm with space group $P3121(152)$ that is consistent with literature data (ICDD reference no. 01-079-0736). CoFeTe-2 showed a few additional peaks with amplification in the intensity of parent peaks compared to Te NTs. The peaks obtained at 2θ value of 47.3, 62.4, 75.3 match with the plane (101), (102), (110) of hexagonal crystal phase of Co (ICDD reference no. 00-001-1278). The peaks at 2θ value of 43.3, 56.9, and 77.6 matches with the plane (102), (201), and (203), respectively of hexagonal crystal phase of cobalt telluride (CoTe) (ICDD reference no. 00-034-0420). The peaks at 2θ value of 45.9, 49.5, 64.0, 77.6 match with the plane (002), (101), (102), (110) respectively of the hexagonal crystal structure of Fe (ICDD reference no. 00-034-0529). The noticeable change observed in XRD patterns of the reactant to the product is due to the growth of Co and Fe NPs on the surface of Te NTs. Since some of the peak positions are the same for Co, CoTe, Fe and Te in the XRD pattern, it is difficult to distinguish unless the rise in intensity of the peak. Te peaks were majorly present since it is predominantly sitting in the backbone. The occurrence of CoTe along with Co NPs on the surface of Te NTs was there because Co^{2+} concentration was high in the reaction, allowing it to interact more with the Te to form an alloy structure as evidenced by the elemental mapping CoFeTe-2 (Fig. 4H). Whereas, Fe^{3+} concentration incorporated in the reaction was very less compared to Co^{2+} failing it to interact with the interior section of Te NTs. As a result, Fe NPs majorly sat on the surface of Te NT, as seen from the elemental mapping of Fe in CoFeTe-2 (Fig. 4I).
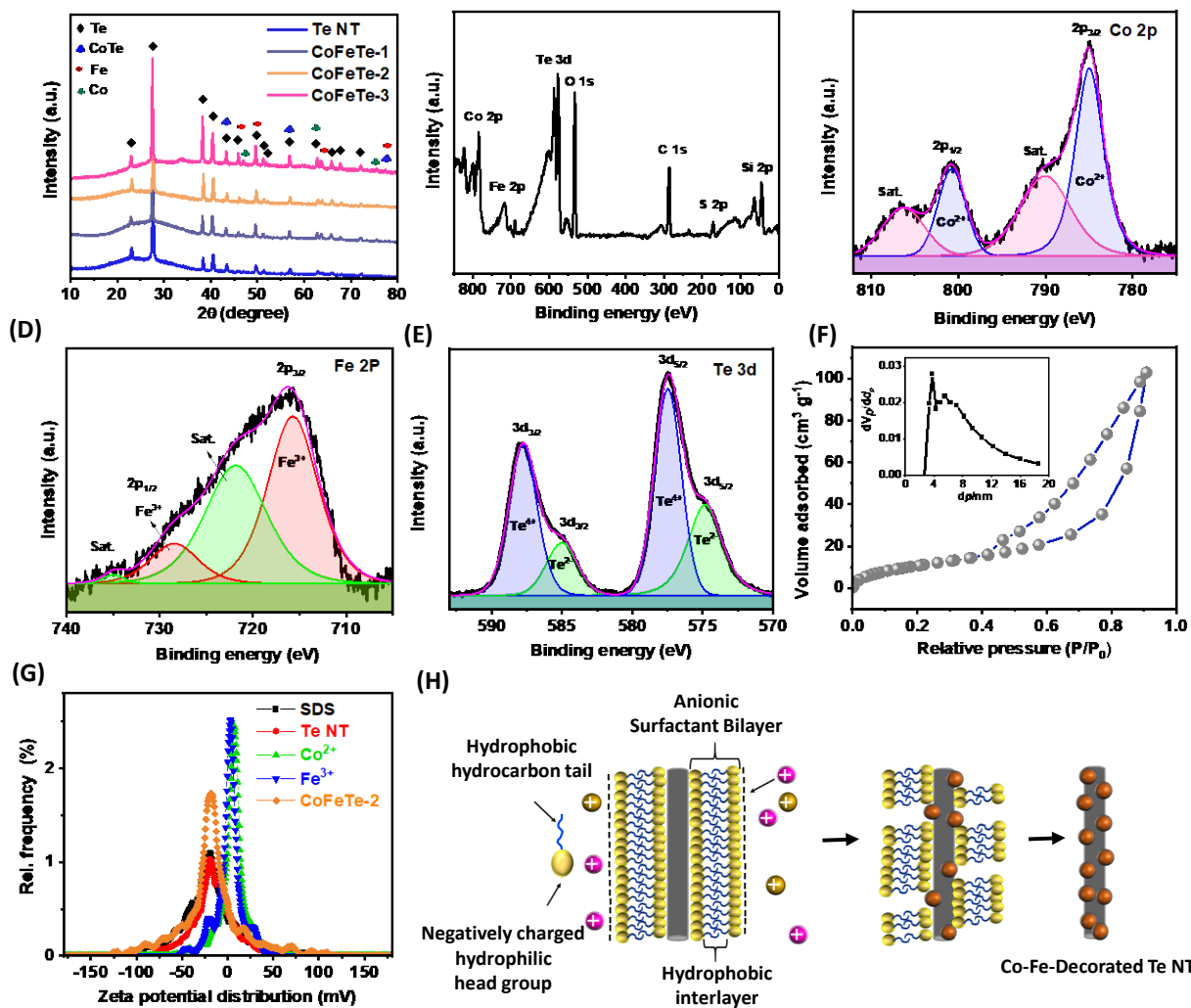
Fig. 5. (A) XRD patterns of all optimized Co-Fe decorated Te NTs and Te NTs, (B) full survey XPS spectrum of CoFeTe-2, (C) magnified XPS spectra of Co 2p, (D) Fe 2p, (E) Te 3d regions, (F) BET analysis of CoFeTe-2, Nitrogen adsorption-desorption isotherms, inset shows pore size distribution, (G) zeta potential measurement, and (H) schematic representation of the formation of Co-Fe decorated Te NT.

Quantitative elemental composition of CoFeTe-2 and valence electronic states of elements like Co, Fe, Te are figured out from XPS analysis, and the full survey spectrum of CoFeTe-2 was

recorded (Fig. 5B). The Co 2p XPS spectrum of CoFeTe-2 splits into four distinct peaks, as shown in Fig. 5C. Two strong peaks were at 784.9 and 800.2 eV, which belongs to Co $2p_{3/2}$ and Co $2p_{1/2}$, respectively representing the existence of Co^{2+} oxidation state [45]. The other peaks centred at 789.8 and 805.9 eV correspond to shakeup satellite peaks [45,46]. For the Fe 2p region, characteristics peaks of Fe $2p_{3/2}$ and Fe $2p_{1/2}$ were observed at a binding energy of 715.6 and 727.8 eV, respectively (Fig. 5D) [47]. In addition to that, two shakeup satellites approximately at the binding energy of 720.8 and 734.2 eV were obtained, indicating the existence of a Fe^{3+} oxidation state [47]. The Te 3d XPS spectrum of CoFeTe-2 (Fig. 5E) splits into four peaks indicating the coexistence of Te^{2-} and Te^{4+}, in which peaks at 584.9 eV in $3d_{3/2}$ and 574.8 eV in Te $3d_{5/2}$ matches with the features of Te^{2-} and peaks at 587.7 eV in $3d_{3/2}$ and 577.4 eV in Te $3d_{5/2}$ matches with the features of Te^{4+} [48].

The surface area of CoFeTe-2 was measured and found to be 43.5 $m^2\,g^{-1}$ from the desorption line using BET isotherm, as shown in Fig. 5F. The pore size distribution of CoFeTe-2 was measured by the BJH method (Fig. 5G), and it shows the maximum number of pores are distributed in the range of 3-4 nm diameter. A type IV isotherm with a hysteresis loop is found in the nitrogen desorption plot, confirming that CoFeTe-2 is a mesoporous surface.
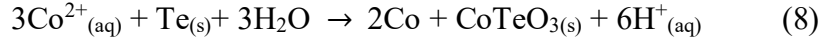

4.2. Mechanism

To determine the mechanism involved in the formation of CoFeTe-2, the surface charge of Co precursor, Fe precursor, SDS, and Te NTs in water medium of similar concentration incorporated during synthesizing CoFeTe-2 was measured using zeta potential measurement. The distribution curve is shown in Fig. 5H, and the zeta potential values are listed in table T1 in the SI.

The aqueous solution of SDS surfactant showed a mean zeta potential of -22.3 mV. The negative surface charge is attributed to its behavior as an anionic surfactant [49]. SDS caps the Te NT by forming a surfactant bilayer in the reaction to avoid agglomeration and directing the growth along one direction [50,51]. Te NTs also adapts to a negative mean zeta potential of -18.9 mV, since it is capped by an anionic surfactant SDS. The mean zeta potential of the metal precursors was calculated; Co $(NO_3)_2.6H_2O$ and $Fe(NO_3)_3.6H_2O$ in aqueous solution showed 0 mV and 1.2 mV, respectively. The zeta potential value of metal precursors became nearly neutral because of the existence of both positively charged Co^{2+}/Fe^{3+} ions and contrary charged NO_3^{2-}/NO_3^{3-} ions neutralizing each other's charges.

The overall mechanism for the formation of CoFeTe-2 can be presented as shown in Fig. H. The hydrophilic polar head group of the surfactant facing water attracts the positive Co^{2+}/Fe^{3+} ions to sit on its surface. The Co^{2+}/Fe^{3+} were reduced to Co/Fe NPs by the residual hydrazine hydrate incorporated during the synthesis of Te NTs. During the process, there is the gradual replacement of surfactant bilayer by Co/Fe NPs. The surface charge of CoFeTe-2 eventually decreases to -16.3 mV compared to its parent Te NTs. Since Fe concentration is less, major of the Fe NPs resides on the surface of Te NT. In contrast, Co interacts on the surface and the interior part of the Te NTs. In addition to that, the sacrificial template characteristic of Te NT accompanies the formation of CoTe. When Te interacts with the Co^{2+} ions, it catalyzes a disproportionate reaction to form Te^{2-} and Te^{4+} and further reacts with Co^{2+} to form CoTe [52]. The reaction mechanism involved in the formation of CoTe is:

$$Te^0 \rightarrow Te^{2-} + Te^{4+} \quad \text{(disproportionate reaction)} \quad (6)$$

$$Co^{2+} + Te^{2-} \rightarrow CoTe \quad (7)$$

$$3Co^{2+}_{(aq)} + Te_{(s)} + 3H_2O \rightarrow 2Co + CoTeO_{3(s)} + 6H^+_{(aq)} \qquad (8)$$

$$2Co + 2Te \rightarrow 2CoTe \qquad (9)$$

The overall structure of Co-Fe decorated Te NTs resembles to its parent precursor Te NT used as a template. However, the tubular morphology generates new NPs upon its surface, increasing the diameter.

4.3. Electrochemical study of Co-Fe decorated Te NTs.

The supercapacitor performance of the optimized electrodes was recorded first in a three-electrode setup in the working electric potential range of 0 to 0.58 V in 4 M KOH aqueous electrolyte. A limited working window of 0.58 V was fixed due to the occurrence of oxygen evolution reaction in the high potential range.[47] To finalize the better electrode from the different optimal ratio of Co/Fe in Te NT for further study, the CV curves at a scan rate of 80 mV s^{-1} obtained from the respective electrodes are plotted (Fig. 6A). Moreover, the contribution of current collector Ni foam was investigated and shown in Fig. 6A. The capacitive performance of electrodes could be figured out from the region covered by the CV curve. Comparing the curve area of all the optimized Co-Fe decorated Te NTs electrodes with Ni Foam, Ni foam showed a very low integral area, confirming major electrochemical performance is contributed from the synthesized Co-Fe decorated Te NTs. All optimized electrodes showed clear redox peaks indicating the charge storage mechanism is battery-type Faradaic charge storage [33]. Among all the optimized Co-Fe decorated Te NTs, the CoFeTe-2 covered a large curve area and a high redox peak intensity in the CV curve, convincing it to be a suitable material for further study.
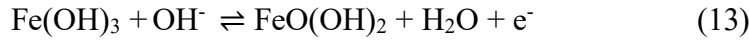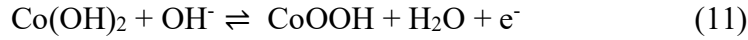
To study the charge/discharge behavior of optimized electrodes, GCD cycles were observed at a constant current density of 7 A g^{-1}. The GCD curves of CoFeTe-1, CoFeTe-2, and CoFeTe-3

depicted the same conclusion predicted from the CV analysis and shown in Fig. 6B. The CoFeTe-2 takes a longer time to discharge than CoFeTe-1 and CoFeTe-3, further confirming its ability to be a better performer than the other two optimized electrodes. The plot of specific capacity vs optimized electrodes (CoFeTe-1, CoFeTe-2 and CoFeTe-3) shown in Fig. 6C obtained using equation 3 at a current density of 7 A g^{-1}, and the values are 48.1 mAh g^{-1}, 84.3 mAh g^{-1} and 19.4 mAh g^{-1}, respectively. Since CoFeTe-2 showed the longest discharge time due to higher specific capacity.

The metal concentration in Co-Fe decorated Te NTs has a significant role in electrochemical performance. The results favoured CoFeTe-2 due to the perfect decoration of Co/Fe NPs without any agglomeration of NTs when the Te: metal precursor (M) concentration ratio is 6:1. The tubular structure with a high active surface area of CoFeTe-2 allows a greater number of electrolyte ions to enter into the core structure of the electrode, resulting in high Faradaic redox activity. When the concentration of Co and Fe is low (Te:M-12:1), the surface of Te NT does not grow enough of Co/Fe NPs, which could participate in the electrochemical activity as a result of which it could not achieve the sufficient energy storage performance. While at a high concentration of Co and Fe precursor (Te:M-3:1), a greater number of Co/Fe NPs grew, which completely sat and covered the surface of Te NTs. It is believed that there is a replacement of surfactant bilayer with Co/Fe NPs on the surface of Te NT, which eventually results in the agglomeration of electrode material, offering minimal active spots in the energy storage performance.

With this, a detailed electrochemical behavior of CoFeTe-2 was systematically investigated at a potential window of 0 to 0.58 V. The scan rate-dependent CV curves (5 mV s^{-1} to 100 mV s^{-1}) of

CoFeTe-2 were plotted in Fig. 6D. All the CV curves showed a clear redox peak from low scan rate to high scan rate; the intensity of the characteristics redox peaks gradually increased without any disappearance of peaks substantiating good reversibility of CoFeTe-2. In addition to that, there is a small change in the redox peak position due to electrodes' polarization [53]. The specific capacitance obtained from the CV curve at different scan rates (5 mV s^{-1} to 100 mV s^{-1}) is obtained by following equation 1 and reported in the Fig. S2 of SI. A prominent redox peak in CV originates because of a redox shift between Co^{2+} and Fe^{3+} in the Faradaic redox reaction owing to cathodic-anodic interchange among Co^{2+}, Fe^{3+} and electrolyte as per the following reaction [29].

$$Co^{2+} + 2OH^- \rightleftharpoons Co(OH)_2 \qquad\qquad (10)$$

$$Co(OH)_2 + OH^- \rightleftharpoons CoOOH + H_2O + e^- \qquad\qquad (11)$$

$$Fe^{3+} + 3OH^- \rightleftharpoons Fe(OH)_3 \qquad\qquad (12)$$

$$Fe(OH)_3 + OH^- \rightleftharpoons FeO(OH)_2 + H_2O + e^- \qquad\qquad (13)$$

The GCD cycles of CoFeTe-2 NT were obtained between the current densities of 6-10 A g^{-1} (Fig. 6E). The curve showed a clear charge-discharge plateau signifying the electrode's battery-type nature, similar to the CV results [47]. No IR drop was observed during discharging because of the outstanding conductivity of CoFeTe-2 qualified to show outstanding rate capability [54]. The specific capacitance and capacity values concerning each current density were determined using equations 2 and 3, respectively and presented in Fig. 6F and 6G. The specific capacitances of CoFeTe-2 electrode are found to be 1119.2, 1075.3, 1043.8, 1035.2 and 1032.1 F g^{-1} with respect to the current densities of 6, 7, 8, 9, and 10 A g^{-1}, respectively. The specific capacities obtained with CoFeTe-2 electrode are 88.3, 84.3, 83.5, 83.1 and 82.5 mA h g^{-1} with respect to the current densities of 6, 7, 8, 9 and 10 A g^{-1}, respectively.
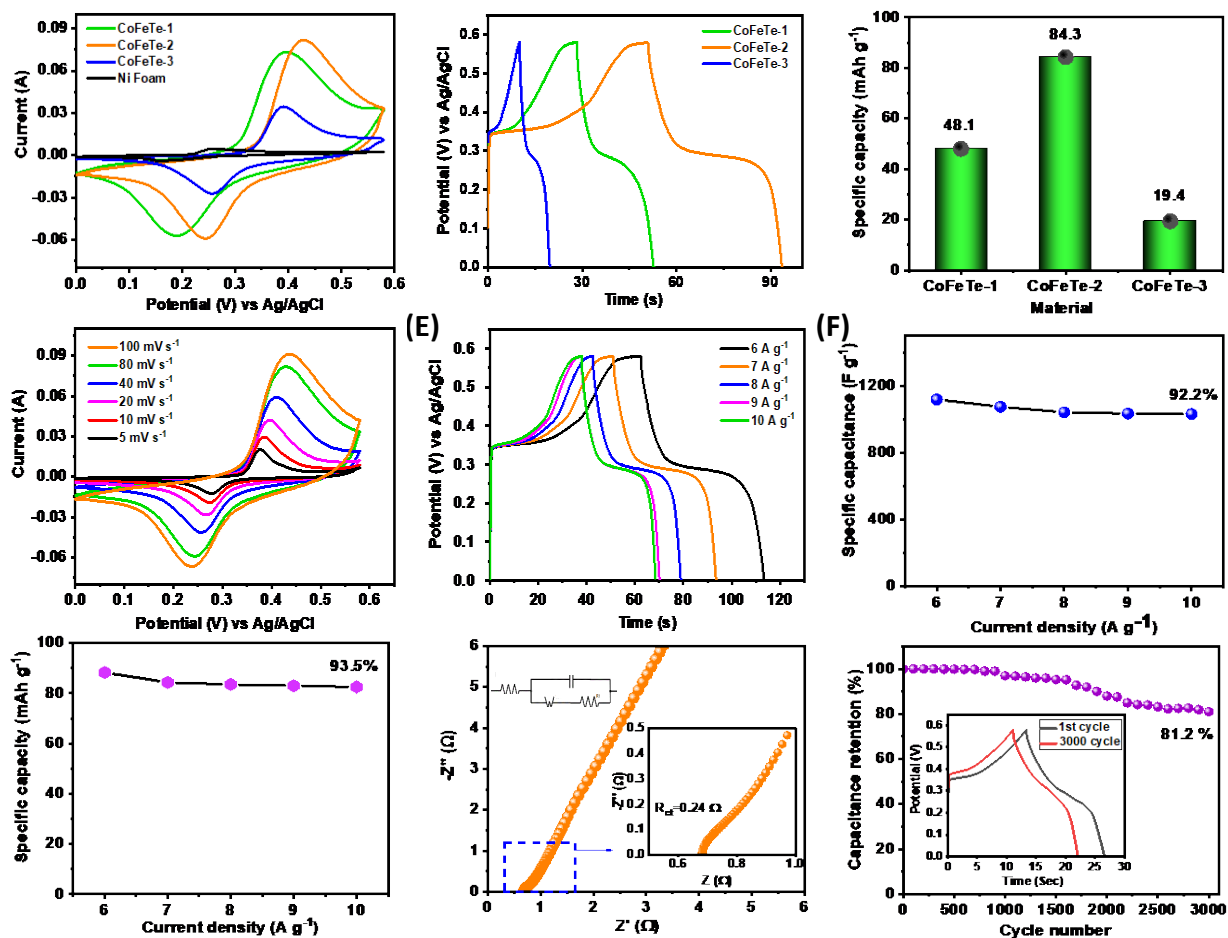
Fig. 6. (A) CV at 80 mV s^{-1}, (B) GCD at 7 A g^{-1}, (C) specific capacity of all optimized electrodes with different Co-Fe ratio on Te NTs, (D) CV curves of the CoFeTe-2 electrode at various scan rates, (E) GCD curves of the CoFeTe-2 electrode at various current densities, (F) specific capacitance and (G) specific capacity of the CoFeTe-2 electrode at different current density, (H) EIS curve of CoFeTe-2 electrode, and (I) cyclic stability of the CoFeTe-2 electrode for 3000 cycles in three-electrode system.

The excellent rate capability of the CoFeTe-2 electrode is confirmed by 92.2 % capacitance retention at a high current density of 10 A g^{-1}. The steady lowering in specific capacitance values with respect to increasing current density is due to the minimal redox reaction kinetics at higher

current density. If the current density is low, the electrolyte ions get adequate time to interact with the outer and inner surface of the electrode, whereas increasing the current density, the electrolyte ions get lesser interaction time and fail to interact sufficiently with the electrode material [32]. With the help of the electrochemical impedance spectroscopy (EIS) test, the capacitive or resistive behavior of the CoFeTe-2 electrode was analyzed and represented in Fig. 6H. Nyquist plot of CoFeTe-2 was recorded between 0.1 to 100000 Hz at a voltage of 5 mV. The solution resistance (R_s) is measured from the horizontal intercept on the X-axis from the EIS curve. While the semicircular region in the high-middle-frequency range denotes the Faradic charge transfer resistance (R_{ct}) estimated from the semicircle diameter. Additionally, a straight line in the lower frequency range in the Nyquist plot resembles the Warburg impedance that originates because of the diffusion of ions inside the electrode material [23]. The electrode showed R_s value of 0.68 Ω and R_{ct} value of 0.24 Ω. The low R_{ct} value indicates superior electrode conductivity, and Randle's equivalent circuit model (inset) shows the fitted circuit.

The cyclic stability is an essential parameter for studying electrode materials' applicability in energy storage devices. A good electrochemical characteristic of CoFeTe-2 was confirmed when a cyclic stability test for 3000 cycles was done at a current density of 15 A g^{-1} (Fig. 6I). CoFeTe-2 obtained a capacitance retention of 81.2% after 3000 cycles. The first and last galvanostatic charge-discharge curves were compared and plotted (inset of Fig. 6I), preserving its charge-discharge plateau even after 3000 cycles. Phenomenal electrochemical properties are observed from Co-Fe decorated Te NTs for the following reasons: (1) The amalgam of two transition metals with conductive Te template in the backbone ignited the reversible redox reaction rate, which eventually resulted in high energy storage. (2) The well-grown Te tubular architect has a large surface area with a dense interpenetrating network, as well as high conductivity, allowing for faster electron

transport and less diffusion space. (3) Moreover, during the decoration process of Co and Fe, it doesn't affect the parent tubular morphology instead, there is a rise in surface area with the bulging out of NPs growth. This provides adequate surface area and effective contact among the electrically active spots of electrode and electrolyte ions to adsorb. The CoFeTe-2 becomes a suitable electrode choice for energy storage performance, benefiting from these advantages mentioned above.

4.4. Working mechanism of CoFeTe-2 electrode

To determine and understand the mechanism during the charge storage process of CoFeTe-2 electrode, the CV curves were in-depth examined. The peak current and scan rate have an exponential relation, also known as power-law and represented as follow:

$$i = a\upsilon^b \qquad (12)$$

$$\log i = b\log(\upsilon) + \log a \qquad (13)$$

In which the unit for "i" is "A", υ is "V s^{-1}" and a, b are the variable parameters [55,56]. The underlying charge storage mechanism occurring inside the electrode material could be figured out from the b value, determined from the slope of the fitted line plotted between log (peak current) vs log (scan rate). The b value getting near to 1 indicates the storage mechanism would be a double layer charge-discharge process and capacitive. Whereas the value of b gets near 0.5, it indicates a battery type Faradaic charge storage process is occurring. The b values obtained with respect to cathodic and anodic plots (Fig. 7A) are 0.49 and 0.56, respectively, confirming the CoFeTe-2 electrode to be more battery-type electrode material. In the plot between peak current vs square root of scan rate (Fig. 7B), a diffusion-control in the insertion of electrolyte ions during Faradaic reaction of the electrode was analyzed as a linear relationship was maintained.

For further verification of charge storage mechanism CV plot was studied in detail. According to the theoretical model proposed by Dunn and coworkers equation 12 could be divided as:

$$i(V) = k_1 \upsilon + k_2 \upsilon^{0.5} \qquad (14)$$

In which at a fixed voltage (V) "i" is current, "υ" is the scan rate, k_1 and k_2 are two constants. To determine the k_1 and k_2 values, a plot of i vs $\upsilon^{0.5}$ is plotted in which the slope and the intercept of the plot give the k_1 and k_2 values [57,58]. The k values are calculated with the method mentioned above for different scan rates at different voltages and employed in equation 14 to obtain the capacitive and diffusive controlled contribution in the total capacity of the electrode material. Fig.7C represents the capacitive and diffusive contribution in the CV curve at a scan rate of 40 mV s^{-1}. The figure shows that the electrode material is majorly storing energy by diffusive controlled process, which matches with the experimental data obtained. The capacitive and diffusive contribution percent at different scan rates was also measured, and the corresponding bar graph is represented in Fig. 7D. With the increase in scan rate from 5 to 100 mV s^{-1}, the capacitive contribution of CoFeTe-2 increased. At the scan rate of 5 mV s^{-1}, the diffusive contribution was 94.2%, while capacitive contribution was very low at 5.8%. As the scan rate increased to 100 mV s^{-1}, the capacitive contribution eventually rose to 31.1%, while the diffusive contribution became 68.9%. This indicates that at a low scan rate, the battery type positive electrode CoFeTe-2 acquires sufficient time to diffuse into the electrode surface and complete the faradaic redox reaction resulting in higher diffusion percentage contribution from overall capacity. Whereas at a high scan rate, less time is available, which favors more physical adsorption of the charges between the electrode-electrolyte interface and results in more capacitive percent. Hence, these observations confirm the device constitutes both battery and supercapacitor type behavior.
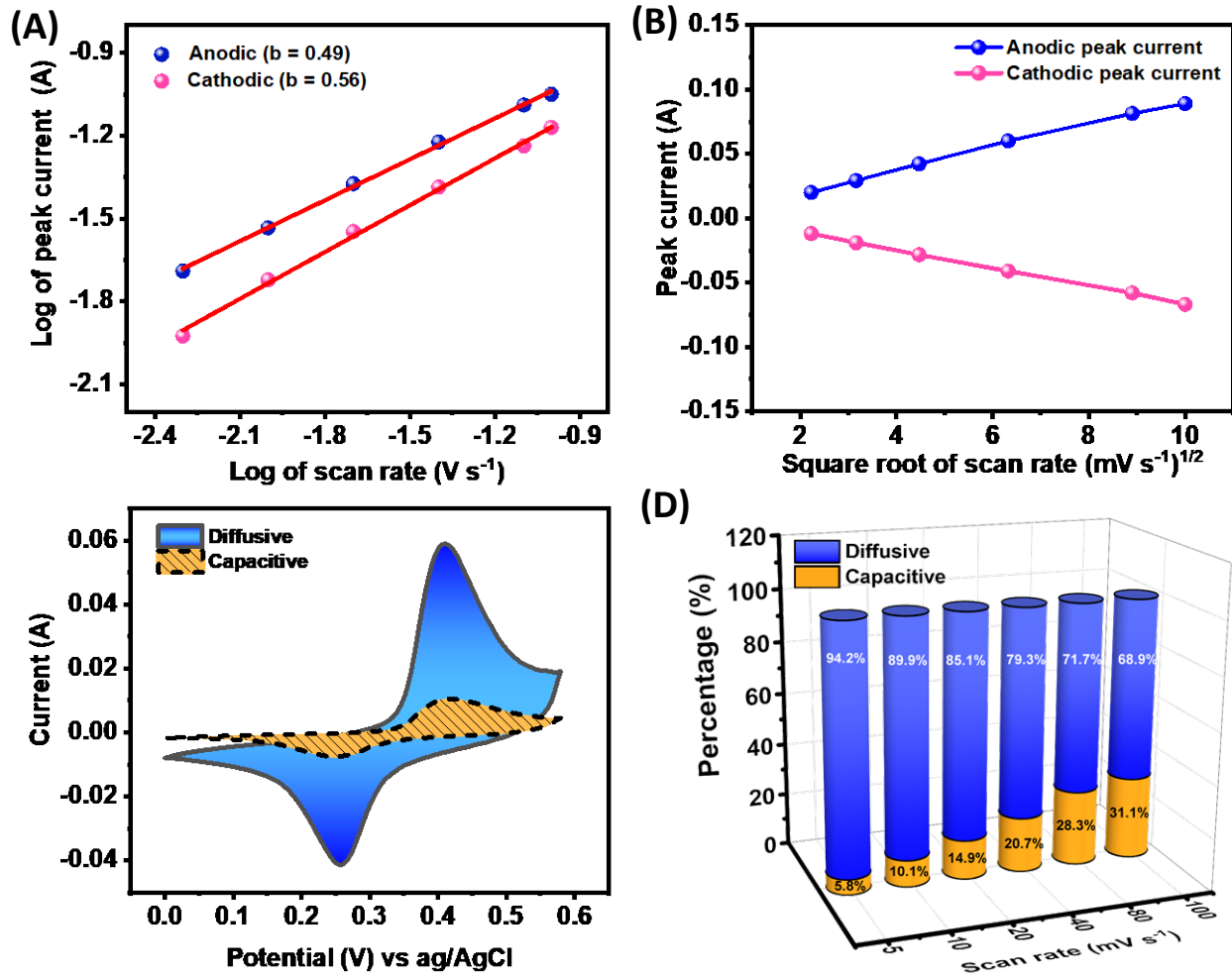
Fig. 7. (A) Function of log (peak current) vs log (scan rate), (B) plot of the square root of scan rate vs. peak current, (C) comparison of capacitive and diffusive controlled contribution in cyclic voltammetry curve at a scan rate of 40 mV s^{-1}, and (D) bar plot displaying capacitive and diffusive controlled contribution percent at different scan rate.

4.5. Performance of CoFeTe-2//AC assembly

An asymmetric setup of CoFeTe-2 with AC was assembled to study its applicability in real-time energy storage applications. When a battery type and EDLC type electrode are combined to form HSC, the power density can possibly be tuned to a higher value without suppressing its energy

density performance. Thus, when arranged in an asymmetric setup, a battery-type CoFeTe-2 electrode works as a positive electrode and an EDLC type AC electrode as a negative electrode (Fig. 8A) [59]. To explore AC's electrochemical performance and working potential window, CV and GCD analysis was collected in a three-electrode system in 4 M KOH and shown in SI (Fig. S3A-C). The CoFeTe-2 and AC operate in different potential windows; CoFeTe-2 becomes active in the potential range of 0 to 0.58 V, whereas AC is active in the potential range of 0 to -1 V (Fig. 8B). With this, the potential window can be extended till 1.58 V for asymmetric assembly of CoFeTe-2//AC. Mass balance of active material is essential to enhance the performance of asymmetric supercapacitors. Hence, the mass of the electrodes was balanced based on the equation (15).

$$\frac{m_+}{m_-} = \frac{C_m^- \Delta V^-}{C_m^+ \Delta V^+} \qquad (15)$$

From the equation, m_+ and m_- represents the mass of active electrodes, C_m^- and C_m^+ are the specific capacitance, ΔV^- and ΔV^+ are the working potential window of the positive and negative electrodes, respectively. Balancing the equation with respect to two electrodes, the mass of AC obtained was ~1.2 mg.

Fig. S4A presents the optimization of asymmetric assembly in different potential windows (1 to 1.58 V). Keeping a constant scan rate of 100 mV s^{-1} and extending the CV curve from 1.58 V to a higher window eventually results in oxygen evolution with a high rise in the current. The curve shape remains unchanged when the potential window is optimized in the range from 1 to 1.58 V, indicating 1.58 V to be a suitable working potential window for asymmetric assembly. Similarly, the GCD curves were obtained by varying the potential ranges from 1 to 1.58 V (Fig. S4B) at a

current density of 3 A g^{-1}. It is noted that the GCD curves obtained at lower potential showed a triangular shape, corroborating the capacitive mechanism to be dominant in the lower potential window. But the shape of GCD cycles changes when the higher potential window is fixed, depicting a mixed mechanism in the charge storage process [33].

Owing to the results mentioned above, the detailed electrochemical analysis of CoFeTe-2//AC was further studied in the optimized potential window of 1.58 V. In Fig. 8 C, the CV curve recorded a varying scan rate from 5 mV s^{-1} to 100 mV s^{-1}. In each of the curves, a partial redox peak appeared because of the presence of battery type CoFeTe-2 electrode, indicating the battery type CoFeTe-2 to be central in the storage mechanism. The GCD cycles were obtained via varying the current densities extending from 0.9 A g^{-1} to 4 A g^{-1} at a fixed potential window of 1.58 V and are presented in Fig. 8D. From the discharging time of GCD analysis, the specific capacitance values for the HSC device was calculated at different current densities following equation 2 and plotted in Fig. 8E. The specific capacitance values are 179.2, 153.8, 110.8, 60.2, and 14.1 F g^{-1} at 0.9, 1, 2, 3 and 4 A g^{-1}, respectively. Fig. S5 shows the specific capacity vs current density calculated using equation 3, and the values obtained are 48.7, 34.7, 30.1, 14.1, 3.7 mAh g^{-1}corresponding to 0.9, 1, 2, 3 and 4 A g^{-1}, respectively.
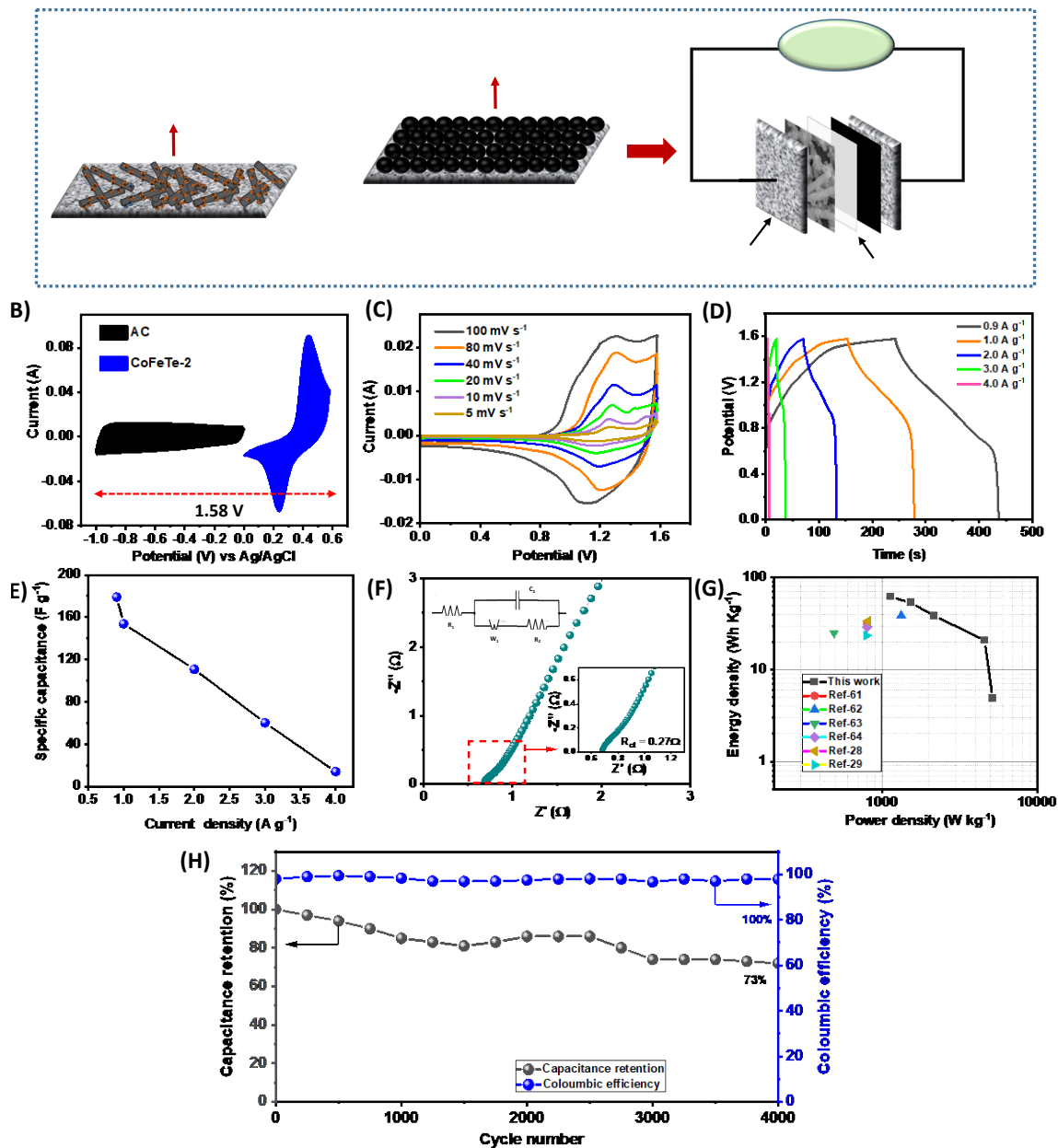
Fig. 8. (A) Schematic representation of asymmetric assembly, (B) CV curves at a scan rate of 100 mV s^{-1} showing the potential working window of AC and CoFeTe-2 respectively, (C) CV, (D) GCD, (E) specific capacitance vs current density for CoFeTe-2//AC, (F) EIS Nyquist curve of CoFeTe-2//AC with circuit fitting, (G) Ragone plot of CoFeTe-2//AC as compared to other reported constituents, and (H) Stability test of the CoFeTe-2 electrode for 4000 cycles in two-electrode system.

Moreover, the device was tested for EIS, and the R_{ct} of 0.27Ω was obtained, clearly signifying the exceptional electrochemical conductivity of the assembly (Fig. 8F). A small R_{ct} might be developed because of the significant interaction of the electrolyte ions with the hydrophilic surface of CoFeTe-2 [60]. Furthermore, based on the GCD curves, the energy density and power density of CoFeTe-2//AC were evaluated using equations 5 and 6 and their Ragone plot is shown in Fig. 8G. HSC reached an utmost energy density of 62.1 Wh Kg^{-1} at a power density of 1138.2 W Kg^{-1}. And even on reaching a high-power density of 5167 W kg^{-1} the electrode could maintain an energy density of 4.8 Wh Kg^{-1}. The energy density and power density received from the anticipated CoFeTe-2//AC device was superior to earlier reported metal chalcogenides-based electrodes for example, $MnCo_2S_4$//rGO (31.3 Wh kg^{-1} at 800 W kg^{-1}) [61], $NiCo_2S_4$//rGO (38.64 Wh kg^{-1} at 1.33 kW kg^{-1}) [62], $NiCo_2Se_4$ //AC (25.0 Wh kg^{-1} at 490 W kg^{-1}) [63], $(Ni_{0.33}Co_{0.67})Se_2$ (29.1 Wh kg^{-1} at 800 W kg^{-1}) [64], NiTe//AC (33.6 Wh Kg^{-1} at 807.1 W Kg^{-1}) [28], CoTe//AC (23. 5 W h kg^{-1} at 793.5 W kg^{-1}) [29]. A comparative study of previously reported monometallic Co decorated Te NTs and other metal chalcogenides electrode with the present work is summarized in Table 2, which indicates the CoFeTe-2//AC to be efficient compared to other reported metal chalcogenides. Finally, the suitability of the electrode prepared in real-time was analyzed by performing a stability test up to 4000 continuous cycles at a current density of 15 A g^{-1} as presented in Fig. 8H. It can be observed for the first 2000 cycles, the capacitance retention endured at 85%. On unceasing the stability test till 4000 cycles, the capacitance retention remains 73% of its initial capacitance. Meanwhile, the coulombic efficiency remained ~100% after 4000 cycles, establishing the first-rate electrochemical reversibility of the fabricated device. FESEM images of the electrode shown in Fig. S6A and B were investigated before and after 4000 cycles and revealed strong structural

stability. The tube-like structures of CoFeTe-2 remain unaltered with slight surface transformation because of the surface charging-discharging process.

Table 2 A comparative study of the previously reported metal chalcogenides and present work.

Material	Morphology	Method	Specific capacitance (2-electrode) $F\ g^{-1}$	Energy density (Wh Kg^{-1})	Reference
$MnCo_2S_4$	Nanowires	Hydrothermal	88.0	31.3	61
$NiCo_2S_4$	Nanoflakes	Hydrothermal-sulfurization	111.5	38.6	62
$NiCo_2Se_4$	Nanotubes	Hydrothermal-selenization	70.2	25.0	63
$(Ni_{0.33}Co_{0.67})Se_2$	Hollow sphere	Hydrothermal-selenization	81.9	29.1	64
Cu-Co-Se	Microsphere	Solvothermal-selenization	-	32.4	65
$Ni@Ni_{0.8}Co_{0.2}Se$	Nanowires	Solvothermal	86	17	66
CoTe	Nanosheets	Hydrothermal	67.3	23.5	29
NiTe	Rod	Hydrothermal	94.6	33.6	28
Co decorated Te	Nanotube	Wet chemical	147	51.1	37
Co-Fe decorated Te	**Nanotube**	**Wet chemical**	**179.2**	**62.1**	**This work**

5. Conclusion

We synthesized Co-Fe decorated Te NTs by adapting a wet chemical approach. Te NTs play a sacrificial template role for the uniform decoration of Co/Fe NPs on Te NT. Three different compositions of Co-Fe decorated Te NTs obtained and optimized by tuning the concentrations of Co^{2+} and Fe^{3+} for electrochemical performances. CoFeTe-2 delivered the highest specific capacitance of 179.2 F g^{-1} (48.7 mA h g^{-1}) at a current density of 0.9 A g^{-1} with the energy density of 62.1 Wh kg^{-1} at a power density of 1138.2 W Kg^{-1} in a two-electrode system (CoFeTe-2//AC). Moreover, the constructed electrode was subjected to 4000 cycles of cyclic stability test, which achieved capacitance retention of 73%. The exceptional electrochemical performance of CoFeTe-2 was attributed to its tubular template structure, conducting Te at the backbone, high surface area and strong synergistic effect between Co, Fe, and Te. With the findings of our study, we believe that the Co-Fe decorated Te NTs will be suitable electrode material for the future application of energy storage devices.

Notes

The authors declare no competing financial interest.

Reference

1. H.E. Ruda, J.C. Polanyi, J.S. Yang, Z. Wu, U. Philipose, T. Xu, S. Yang, K. Kavanagh, J. Liu, L. Yang, Developing 1D nanostructure arrays for future nanophotonics, Nanoscale Research Letters 1(2) (2006) 99-119.

2. K.J. Choi, H.W. Jang, One-dimensional oxide nanostructures as gas-sensing materials: review and issues, Sensors 10(4) (2010) 4083-4099.

3. P. Bhol, M. Bhavya, S. Swain, M. Saxena, A.K. Samal, Modern chemical routes for the controlled synthesis of anisotropic bimetallic nanostructures and their application in catalysis, Frontiers in Chemistry 8 (2020) 357.

4. S. Swain, B. MB, V. Kandathil, P. Bhol, A.K. Samal, S.A. Patil, Controlled Synthesis of Palladium Nanocubes as an Efficient Nanocatalyst for Suzuki–Miyaura Cross-Coupling and Reduction of p-Nitrophenol, Langmuir 36(19) (2020) 5208-5218.

5. Z. Zhang, Z. Kang, Q. Liao, X. Zhang, Y. Zhang, One-dimensional ZnO nanostructure-based optoelectronics, Chinese Physics B 26(11) (2017) 118102.

6. D. Ye, Y. Ding, Y. Duan, J. Su, Z. Yin, Y.A. Huang, Large-Scale Direct-Writing of Aligned Nanofibers for Flexible Electronics, Small 14(21) (2018) 1703521.

7. J.R. Miller, P. Simon, Electrochemical capacitors for energy management, Science Magazine 321(5889) (2008) 651-652.

8. L. Zhang, X. Hu, Z. Wang, F. Sun, D.G. Dorrell, A review of supercapacitor modeling, estimation, and applications: A control/management perspective, Renewable and Sustainable Energy Reviews 81 (2018) 1868-1878.

9. N. Wu, X. Bai, D. Pan, B. Dong, R. Wei, N. Naik, R.R. Patil, Z. Guo, Recent advances of asymmetric supercapacitors, Advanced Materials Interfaces 8(1) (2021) 2001710.

10. Y. Zhang, H. Hu, Z. Wang, B. Luo, W. Xing, L. Li, Z. Yan, L. Wang, Boosting the performance of hybrid supercapacitors through redox electrolyte-mediated capacity balancing, Nano Energy 68 (2020) 104226.

11. Q. Wang, Z. Wen, J. Li, A hybrid supercapacitor fabricated with a carbon nanotube cathode and a TiO_2–B nanowire anode, Advanced Functional Materials 16(16) (2006) 2141-2146.

12. T. Brousse, D. Bélanger, J.W. Long, To be or not to be pseudocapacitive?, Journal of The Electrochemical Society 162(5) (2015) A5185.

13. S. Fleischmann, J.B. Mitchell, R. Wang, C. Zhan, D.-e. Jiang, V. Presser, V. Augustyn, Pseudocapacitance: from fundamental understanding to high power energy storage materials, Chemical Reviews 120(14) (2020) 6738-6782.

14. Y.H. Wang, K.J. Huang, X. Wu, Recent advances in transition-metal dichalcogenides based electrochemical biosensors: A review, Biosensors and Bioelectronics 97 (2017) 305-316.

15. Z. Tang, H. Yang, Transition metal chalcogenides for energy storage and conversion, Advanced Nanomaterials for Electrochemical-Based Energy Conversion and Storage, Elsevier2020, pp. 355-391.

16. T. Heine, Transition metal chalcogenides: ultrathin inorganic materials with tunable electronic properties, Accounts of chemical research 48(1) (2015) 65-72.

17. J. Theerthagiri, K. Karuppasamy, G. Durai, A.U.H.S. Rana, P. Arunachalam, K. Sangeetha, P. Kuppusami, H.-S. Kim, Recent advances in metal chalcogenides (MX; X= S, Se) nanostructures for electrochemical supercapacitor applications: a brief review, Nanomaterials 8(4) (2018) 256.

18. M. Liu, Z. Wang, J. Liu, G. Wei, J. Du, Y. Li, C. An, J. Zhang, Synthesis of few-layer 1T′-MoTe 2 ultrathin nanosheets for high-performance pseudocapacitors, Journal of Materials Chemistry A 5(3) (2017) 1035-1042.

19. J. Guo, X. Zhang, Y. Sun, X. Zhang, L. Tang, X. Zhang, Double-shell CuS nanocages as advanced supercapacitor electrode materials, Journal of Power Sources 355 (2017) 31-35.

20. J. Li, D. Chen, Q. Wu, Facile synthesis of CoS porous nanoflake for high performance supercapacitor electrode materials, Journal of Energy Storage 23 (2019) 511-514.

21. Y. Zhang, N. Cao, S. Szunerits, A. Addad, P. Roussel, R. Boukherroub, Fabrication of ZnCoS nanomaterial for high energy flexible asymmetric supercapacitors, Chemical Engineering Journal 374 (2019) 347-358.

22. Y. Zhao, Z. Shi, H. Li, C.-A. Wang, Designing pinecone-like and hierarchical manganese cobalt sulfides for advanced supercapacitor electrodes, Journal of Materials Chemistry A 6(26) (2018) 12782-12793.

23. Y. Miao, Y. Sui, D. Zhang, J. Qi, F. Wei, Q. Meng, Y. He, Z. Sun, Y. Ren, Polyhedral NiCoSe$_2$ synthesized via selenization of metal-organic framework for supercapacitors, Materials Letters 242 (2019) 42-46.

24. Y. Chen, C. Jing, X. Fu, M. Shen, K. Li, X. Liu, H.-C. Yao, Y. Zhang, K.X. Yao, Synthesis of porous NiCoS nanosheets with Al leaching on ordered mesoporous carbon for high-performance supercapacitors, Chemical Engineering Journal 384 (2020) 123367.

25. A. Coker, T. Lee, T. Das, Investigation of the electronic properties of tellurium—energy-band structure, Physical Review B 22(6) (1980) 2968.

26. R.S. Caldwell, H. Fan, Optical properties of tellurium and selenium, Physical Review 114(3) (1959) 664.

27. P. Mohanty, T. Kang, B. Kim, J. Park, Synthesis of single crystalline tellurium nanotubes with triangular and hexagonal cross sections, The Journal of Physical Chemistry B 110(2) (2006) 791-795.

28. P. Zhou, L. Fan, J. Wu, C. Gong, J. Zhang, Y. Tu, Facile hydrothermal synthesis of NiTe and its application as positive electrode material for asymmetric supercapacitor, Journal of Alloys and Compounds 685 (2016) 384-390.

29. B. Ye, C. Gong, M. Huang, Y. Tu, X. Zheng, L. Fan, J. Lin, J. Wu, Improved performance of a CoTe//AC asymmetric supercapacitor using a redox additive aqueous electrolyte, RSC advances 8(15) (2018) 7997-8006.

30. L.K. Bommineedi, T.K. Shivasharma, B.R. Sankalp, Mixed phase $FeTe:Fe_2TeO_5$ nanopebbles through solution chemistry: Electrochemical supercapacitor application, Ceramics International (2021).

31. P. Yu, W. Fu, Q. Zeng, J. Lin, C. Yan, Z. Lai, B. Tang, K. Suenaga, H. Zhang, Z. Liu, Controllable Synthesis of Atomically Thin Type-II Weyl Semimetal WTe_2 Nanosheets: An Advanced Electrode Material for All-Solid-State Flexible Supercapacitors, Advanced Materials 29(34) (2017) 1701909.

32. M. Manikandan, K, Subramani, S. Dhanuskodi, M. Sathish, One-Pot Hydrothermal Synthesis of Nickel Cobalt Telluride Nanorods for Hybrid Energy Storage Systems, Energy & Fuels 35(15) (2021) 12527–12537.

33. N. Jayababu, S. Jo, Y. Kim, D. Kim, Novel Conductive Ag-Decorated NiFe Mixed Metal Telluride Hierarchical Nanorods for High-Performance Hybrid Supercapacitors, ACS Applied Materials & Interfaces 13(17) (2021) 19938-19949.

34. Y.C. Chen, Y.G. Lin, Y.K. Hsu, S.C. Yen, K.H. Chen, L.C. Chen, Novel Iron Oxyhydroxide Lepidocrocite Nanosheet as Ultrahigh Power Density Anode Material for Asymmetric Supercapacitors, Small 10(18) (2014), 3803-3810.

35. P.A. Frey, G.H. Reed, The ubiquity of iron, ACS Chemical Biology 7(9) (2012) 1477-1481.

36. S. Verma, A. Khosla, S. Arya, Performance of Electrochemically Synthesized Nickel-Zinc and Nickel-Iron (Ni−Zn//Ni−Fe) Nanowires as Battery Type Supercapacitor, Journal of The Electrochemical Society 167(72) (2020) 120527.

37. P. Bhol, S. Swain, S. Jena, K. Bhatte, C.S. Rout, M. Saxena, A.H. Jadhav, A.K. Samal, Co-Decorated Tellurium Nanotubes for Energy Storage Applications, ACS Applied Nano Materials 4(9) (2021) 9008.

38. B. Mayers, Y. Xia, One-dimensional nanostructures of trigonal tellurium with various morphologies can be synthesized using a solution-phase approach. Journal of Materials Chemistry 12(6) (2002) 1875-1881.

39. H.S. Qian, S.H. Yu, J.Y. Gong, L.B. Luo, L.F. Fei, High-quality luminescent tellurium nanowires of several nanometers in diameter and high aspect ratio synthesized by a poly (vinyl pyrrolidone)-assisted hydrothermal process, Langmuir 22(8) (2006) 3830-3835.

40. D. Qin, J. Zhou, C. Luo, Y. Liu, L. Han, Y. Cap, Surfactant-assisted synthesis of size controlled trigonal Se/Te alloy nanowires, Nanotechnology 17(3) (2006) 674

41. A.K. Samal, T. Pradeep, Room-temperature chemical synthesis of silver telluride nanowires, The Journal of Physical Chemistry C 113(31) (2009) 13539-13544.

42. Q. Gao, C.Q. Huang, Y.M. Ju, M.R. Gao, J.W. Liu, D. An, C.H. Cui, Y.R. Zheng, W.X. Li, S.H. Yu, Phase-selective syntheses of cobalt telluride CoTe for efficient oxygen evolution catalysts, AngewandteChemie International Edition 56(27) (2017) 7769-7773.

43. J.M. Song, Y.Z. Lin, Y.J. Zhan, Y.C. Tian, G. Liu, S.H. Yu, Superlong high-quality tellurium nanotubes: synthesis, characterization, and optical property, Crystal Growth and Design 8(6) (2008) 1902-1908.

44. G. Xi, Y. Peng, W. Yu, Y. Qian, Synthesis, characterization, and growth mechanism of tellurium nanotubes, Crystal growth & design 5(1) (2005) 325-328.

45. L. Hou, Y. Shi, C. Wu, Y. Zhang, Y. Ma, X. Sun, J. Sun, X. Zhang, C. Yuan, Monodisperse metallic $NiCoSe_2$ hollow sub-microspheres: formation process, intrinsic charge-storage mechanism, and appealing pseudocapacitance as highly conductive electrode for electrochemical supercapacitors, Advanced Functional Materials 28(13) (2018) 1705921.

46. J. Lin, H. Wang, Y. Yan, X. Zheng, H. Jia, J. Qi, J. Cao, J. Tu, W. Fei, J. Feng, Core-branched $CoSe_2$/Ni $_{0.85}$ Se nanotube arrays on Ni foam with remarkable electrochemical performance for hybrid supercapacitors, Journal of Materials Chemistry A 6(39) (2018) 19151-19158.

47. I. Hussain, J.M. Lee, S. Iqbal, H.S. Kim, S.W. Jang, J.Y. Jung, H.J. An, C. Lamiel, S.G. Mohamed, Y.R. Lee, J.J. Shim, Preserved crystal phase and morphology: electrochemical influence of copper and iron co-doped cobalt oxide and its supercapacitor applications, Electrochimica Acta 340 (2020) 135953.

48. M. Manikandan, S. Dhanushkodi, N. Maheswari, G. Muralidharan, C. Revathi, R.R. Kumar, G.M. Rao, High performance supercapacitor and non-enzymatic hydrogen

peroxide sensor based on tellurium nanoparticles. Sensing and Bio-Sensing Research 13 (2017) 40-48.

49. D.L. Liao, G.S. Wu, B.Q. Liao, Zeta potential of shape-controlled TiO_2 nanoparticles with surfactants, Colloids and Surfaces A: Physicochemical and Engineering Aspects 348(1-3) (2009) 270-275.

50. B. Nikoobhakt, M.A. El-Sayed, Evidence for bilayer assembly of cationic surfactants on the surface of gold nanorods, Langmuir 17(20) (2001) 6368-6374.

51. J. Gao, C.M. Bender, C.J. Murphy, Dependence of the gold nanorod aspect ratio on the nature of the directing surfactant in aqueous solution, Langmuir 19(21) (2003) 9065-9070.

52. B. Gates, B. Mayers, Y. Wu, Y. Sun, B. Cattle, P. Yang, Y. Xia, synthesis and characterization of crystalline Ag_2Se nanotubes through a template-engaged reaction at room temperature, Advanced Functional Materials 12(10) (2002) 679-686.

53. Y. Zhang, J. Xu, Y. Zheng, Y. Zhang, X. Hu, T. Xu, Construction of $CuCo_2O_4@ CuCo_2O_4$ hierarchical nanowire arrays grown on Ni foam for high performance supercapacitors, RSC Advances 7(7) (2017) 3983-3991.

54. Y. Zhang, A. Pan, Y. Wang, X. Cao, Z. Zhou, T. Zhu, S. Liang, G. Cao, Self-templated synthesis of N-doped $CoSe_2$/C double-shelled dodecahedra for high-performance supercapacitors, Energy Storage Materials 8 (2017) 28-34.

55. J. Cao, J. Li, L. Zhou, Y. Xi, X. Cao, Y. Zhange, W. Han, Tunable Agglomeration of Co_3O_4 Nanowires as the Growing Core for In-Situ Formation of Co_2NiO_4 Assembled with Polyaniline-Derived Carbonaceous Fibers as the High-Performance Asymmetric Supercapacitors, Journal of Alloys and Compounds 853 (2021) 157210.

56. B. Ramulu, G. Nagaraju, S. Chandra Sekhar, S.K. Hussain, D. Narsimulu, J.S. Yu, Synergistic effects of cobalt molybdate@ phosphate core–shell architectures with ultrahigh capacity for rechargeable hybrid supercapacitors, ACS applied materials & interfaces 11(44) (2019) 41245-41257.

57. S.B. Xia, S.W. Yu, L.F. Yao, F.S. Li, X. Li, F.X. Cheng, X. Shen, C.K. Sun, H. Guo, J.J. Liu, Robust hexagonal nut-shaped titanium (IV) MOF with porous structure for ultra-high performance lithium storage, Electrochimica Acta 296 (2019) 746-754.

58. M.Z. Iqbal, S.S. Haider, S. Siddique, M.R.A. Karim, S. Zakar, M. Tayyab, M.M. Faisal, M. Sulman, A. Khan, M. Baghayeri, M.A. Kamran, Capacitive and diffusion-controlled mechanism of strontium oxide based symmetric and asymmetric devices, Journal of Energy Storage 27 (2020) 101056.

59. N. Choudhary, C. Li, J. Moore, N. Nagaiah, N. Zhai, Y. Jung, J. Thomas, Asymmetric supercapacitor electrodes and devices, Advanced Materials 27(21) (2017) 1605336.

60. S. Zhang, D. Yang, M. Zhang, Y. Liu, T. Xu, J. Yang, Z.Z. Yu, Synthesis of novel bimetallic nickel cobalt telluride nanotubes on nickel foam for high-performance hybrid supercapacitors, Inorganic Chemistry Frontiers 7(2) (2020) 477-486.

61. S. Liu, S.C. Jun, Hierarchical manganese cobalt sulfide core–shell nanostructures for high-performance asymmetric supercapacitors, Journal of Power Sources 342 (2017) 629-637.

62. F. Lu, M. Zhou, W. Li, Q. Weng, C. Li, Y. Xue, X. Jiang, X. Zeng, Y. Bando, D. Golberg, Engineering sulfur vacancies and impurities in $NiCo_2S_4$ nanostructures toward optimal supercapacitive performance, Nano Energy 26 (2016) 313-323.

63. S. Li, Y. Ruan, Q. Xia, . Morphological modulation of $NiCo_2Se_4$ nanotubes through hydrothermal selenization for asymmetric supercapacitor, Electrochimica Acta 356 (2020) 136837.

64. L. Quan, T. Liu, M. Yi, Q. Chen, D. Cai, H. Zhan, Construction of hierarchical nickel cobalt selenide complex hollow spheres for pseudocapacitors with enhanced performance, Electrochimica Acta 281 (2018) 109-116.

65. S.E. Moosavifard, F. Saleki, A. Mohammadi, A. Hafizi, M.R. Rahimpour, Construction of hierarchical nanoporous bimetallic copper-cobalt selenide hollow spheres for hybrid supercapacitor, Journal of Electroanalytical Chemistry 871 (2020) 114295.

66. K. Guo, S. Cui, H. Hou, W. Chen, L. Mi, Hierarchical ternary Ni–Co–Se nanowires for high-performance supercapacitor device design, Dalton Transactions 45(48) (2016) 19458-19465.

GRAPHICAL ABSTRACT